Conical intersection seam and bound resonances embedded in continuum observed in the photodissociation of thioanisole-d_3

Songhee Han,[a),b)] Jeong Sik Lim,[a),c)] Jun-Ho Yoon,[a)] Jeongmook Lee, So-Yeon Kim, and Sang Kyu Kim[d)]
Department of Chemistry, KAIST, Daejeon 305-701, South Korea

(Received 29 October 2013; accepted 15 January 2014; published online 4 February 2014)

Herein, the multi-dimensional nature of the conical intersection seam has been experimentally revealed in the photodissociation reaction of thioanisole-d_3 ($C_6H_5SCD_3$) excited on S_1, giving $C_6H_5S\cdot(\tilde{A}$ or $\tilde{X}) + \cdot CD_3$ products. The translational energy distribution of the nascent $\cdot CD_3$ fragment, reflecting the relative yields of the $C_6H_5S\cdot(\tilde{A})$ and $C_6H_5S\cdot(\tilde{X})$ products, was measured at each S_1 vibronic band using the velocity map ion imaging technique. Direct access of the reactant flux to the conical intersection seam leads to the increase of the nonadiabatic transition probability resulting in sharp resonances in the $\tilde{X}/\tilde{A}C_6H_5S\cdot$ product branching ratio at several distinct S_1 vibronic bands. The nature of the S_1 vibronic bands associated with such dynamic resonances was clarified by the mass-analyzed threshold ionization spectroscopy. The bound state embedded in continuum generated by the conical intersection is observed as a distinct dynamic resonance, revealing the nature of the nuclear motion responsible for the nonadiabatic coupling of two potential energy surfaces at the conical intersection. The multi-dimensional facets of the conical intersection seam in terms of its detailed structure and dynamic role are discussed with the aid of theoretical calculations.
 [http://dx.doi.org/10.1063/1.4863449]

I. INTRODUCTION

Chemical reactions at a fundamental level involve movement and exchange of electrons and nuclei of participating atoms. This is envisioned by nuclear displacements on multi-dimensional potential energy surfaces which rely on the Born-Oppenheimer approximation.[1] This approximation ties the nuclear motion to the adiabatic potential energy surface where the electronic rearrangement is assumed to be much faster than the nuclear motion. For chemical reactions on closely lying electronically excited states, however, nuclear and electronic motions are not separable. In this case, the nuclear motion is not restricted to the adiabatic potential energy surface, and nonadiabatic transitions among different adiabats take place with significant probabilities.[2–6] For polyatomic molecular systems, conical intersections comprised of nuclear configurations in which two (or more) electronic states are degenerate have been widely accepted as dynamic funnels through which nonadiabatic transitions become facilitated. The conical intersection is defined as a point in the two-dimensional branching plane generated by gradient difference (g) and nonadiabatic coupling (h) vectors, and it actually forms a seam along the ($N^{int}-2$) dimensional intersection space where N^{int} is the number of internal degrees of freedom.[2–6] It is currently a formidable task to determine the full number of nuclear configurations corresponding to the conical intersection seam. This determination, however, can allow for a powerful shortcut in understanding nonadiabatic chemical reactions wherein the full knowledge and elucidation of the whole complex multi-dimensional potential energy surfaces are not required.

The structure and dynamic role of the conical intersection have been subjected to intensive theoretical[2–9] and experimental studies[10–23] for decades. Despite numerous successful theoretical and experimental studies, however, chemists still keenly undertake probing of the conical intersection region more directly. Since conical intersections are often found between reactants and products along the reaction pathway, mainly time-resolved studies have been employed for capturing the nuclear motion in the conical intersection region. In this regard, recent studies of NO_2 excited state dynamics[19] and photoisomerization of rhodopsin[20] are notable real-time studies that clarify the critical role of conical intersections in efficient surface hopping processes. To interrogate the topological aspect of nonadiabatic chemistry, however, one should be able to locate the conical intersection more precisely on the multi-dimensional potential energy surfaces. Importantly, our recent report on the photodissociation dynamics of thioanisole ($C_6H_5SCH_3$)[12] yielded energetic and structural properties of the conical intersection responsible for the nonadiabatic transition of S–CH_3 bond dissociation. A more recent femtosecond report by Stavros and colleagues[14] has provided the temporal dynamic aspect of the same system. Herein, we report the experimental observation of the multi-dimensional facets of the conical intersection seam governing the nonadiabatic chemical reaction of the isotopologue of thioanisole (C_6H_5S–CD_3). The nuclear configurations of the initial reactant flux are extremely critical in controlling

[a)] S. Han, J. S. Lim, and J.-H. Yoon contributed equally to this work.
[b)] Present address: Max Born Institute, Berlin, Germany.
[c)] Present address: Korea Research Institute of Standards and Science, Daejeon, South Korea.
[d)] Author to whom correspondence should be addressed. Electronic mail: sangkyukim@kaist.ac.kr.

nonadiabatic dynamics of the excited electronic states through strong coupling of nuclear and electronic motion. We propose here that the bound state embedded in continuum generated by the conical intersection is observed experimentally for the first time in the photodissociation reaction of a polyatomic system.

II. EXPERIMENT

Thioanisole-d_3 ($C_6H_5SCD_3$) was heated to 35 °C to afford the ~1% mixture of the sample in the helium carrier gas at the total backing pressure of 3 atm. The gas mixture was expanded through a 0.5 mm diameter orifice of the pulsed nozzle valve (General valve 9 series) into vacuum at the repetition rate of 10 Hz with a home-made nozzle driver. The vacuum chamber was differentially pumped by two turbo molecular pumps (Varian, TV 551) backed by a mechanical pump (Varian, DS 602) to maintain the background pressure of 10^{-7} Torr when the nozzle was operated. The visible laser output from a dye laser (Sirah) pumped by a Nd:YAG laser (Spectra Physics, Lab 170) was frequency-doubled by a β-barium borate (BBO) crystal mounted on a home-made auto-tracker to give the tunable UV laser pulse, which was used for the excitation of the jet-cooled thioanisole-d_3. To probe the nascent $\cdot CD_3$ radical, the other dye laser output (Lambda Physik, Scanmate2) pumped by another Nd:YAG laser (Continuum, Surelite-II) was frequency-doubled to generate the UV laser pulse at 333 nm for the (2+1) multiphoton ionization of the $\cdot CD_3$ radical via the zero point (0_0^0) level of the $3p\ ^2A_2''$ Rydberg state. The pump and probe laser pulses were both timely and spatially overlapped in a counter-propagating manner on the molecular beam. As a function of the excitation pump laser frequency, the parent ion signal was monitored in the resonant two-photon ionization (R2PI) spectroscopy, whereas the $\cdot CD_3$ ion signal was taken for obtaining photofragment excitation (PHOFEX) spectra. In both cases, the ion signal was separated in the time-of-flight mass spectrometry according the mass/charge ratio, digitized using the oscilloscope (LeCroy), and stored in a personal computer using a home-made data taking program. To measure translational energy and angular distributions of the nascent $\cdot CD_3$ fragment, the velocity map ion imaging technique[24–26] was employed. Once the nascent CD_3 radical was ionized in the appropriate ion optics, its velocity was mapped on a position-sensitive detector equipped with dual microchannel plates and a P20 phosphor screen (Burle, 3040 FM CT, 40 mm diameter). The pump laser polarization was perpendicular to the time-of-flight axis and parallel to the plane of the detector. Doppler broadening of the $\cdot CD_3$ fragment was within the probe laser bandwidth ($\Delta\tilde{\upsilon} \sim 0.7\ cm^{-1}$). Images on the phosphor screen was acquired by a charge-coupled device (CCD) camera (Hammamatsu) using a gravity event counting method. Three-dimensional images were reconstructed from two-dimensional raw images using the basis-set expansion (BASEX) algorithm.[26] Detailed setup for the velocity map ion imaging had been described earlier.[11,12] Images were averaged for 100 000–720 000 laser shots. For the mass analyzed threshold ionization (MATI) spectroscopy, the excitation laser pulse in the range of 280–290 nm and the ionization laser pulse in the 327–355 nm range were generated by frequency doubling of two independently tunable dye laser outputs pumped by the second harmonic output of a Nd:YAG laser (Continuum, Precision 2). The experimental details for the MATI spectroscopy have been described previously.[27,28] Briefly, the parent molecule was excited to long-lived Rydberg states using the two-color two-photon excitation scheme before being ionized by the pulsed-field ionization technique using the electric pulse of ~160 V/cm with a delay time of ~50 μs after the laser excitation. The MATI ions were accelerated, drifted along the time-of-flight tube, and detected by dual micro-channel plates. The MATI spectra were taken as a function of the ionization laser frequency at fixed excitation energies for specific intermediate states.

A. Computational details

Potential energy curves along each coordinate were calculated at the level of a state-averaged complete active space self-consistent field (SA-CASSCF). An active space associated with 12 electrons distributed into 11 molecular orbitals (MOs) using a 6-311++G(d,p) basis set was used. Second-order multireference perturbation theory (CASPT2) was used for the calculation of some selected energy points in Table I. Gradient difference (g) and nonadiabatic coupling (h) vectors for the degenerate points on the seam and for the

TABLE I. Molecular structural parameters and minimum energies of thioanisole-d_3 at the ground (S_0), first excited (S_1), cationic ground states (D_0), S_1/S_2 MECI, and the lowest point of the conical intersection seam calculated in the reduced dimensionality (CI^{red}) are given. *Ab initio* values are obtained at the (SA4-CASSCF(12,11)/6-311++G(d,p)) level whereas the values in parentheses are after the PT2 correction.

	Equilibrium					
	S_0	S_1		D_0	MECI	CI^{red}
Relative energy (cm^{-1})	0	37 134	38 794[a]	55 098	39 749	40 734
	(0)	(33 487)	(35 187)[a]	(60 988)	(37 552)	(38 649)
d(C–SCD_3) (Å)	1.82	1.79		1.72	1.78	1.81
d(CS–CD_3) (Å)	1.86	1.87		1.87	2.13	2.10
γ(C–S–CD_3) (deg)	102.34	103.13		106.13	102.63	102.84
γ(S–C–$D_{(3)}$) (deg)	105.02	104.91		104.30	101.25	102.65
d(C–C)[b] (Å)	1.40	1.43		1.40	1.42	1.40

[a]The S_1–S_0 vertical excitation energy at the S_0 minimum energy geometry.
[b]Averaged values for the phenyl moiety.

minimum-energy conical intersection (MECI) were calculated using the coupled-perturbed multi-configurational self-consistent field (CP-MCSCF) method. D_0 normal modes of thioanisole-d_3 were calculated at the B3LYP Density Functional Theory (DFT)/6-311++G(3df,3pd) or SA4-CASSCF(11,11)/6-311++G(d,p) level. The displacement vectors of the vibrational modes obtained from the two methods were quite similar while associated vibrational energies were somewhat different. The nuclear configurations spanned by the normal mode are those obtained from the CASSCF calculation. All CASSCF and DFT calculations were performed with MOLPRO (version 2010.1) and the Gaussian 09 program package, respectively.

III. RESULTS AND DISCUSSION

In the S–CD_3 bond dissociation of thioanisole-d_3 (C_6H_5S–CD_3) excited at S_1, two conical intersections are consecutively encountered along the reaction pathway.[12,14] Whereas the S_1 state ($\pi\pi^*$) is bound, the upper-lying S_2 ($\pi\sigma^*$) is repulsive along the S–CD_3 bond elongation coordinate. The resultant S_1/S_2 conical intersection acts as a dynamic channel for the initially bound reactant flux to ride on the repulsive potential energy surface, Fig. 1. The S_0/S_2 conical intersection then acts as the nonadiabatic dynamic funnel at the later stage of the chemical reaction as the S_0 ground state diabatically correlates to the excited state of the phenylthiyl radical, $C_6H_5S\cdot(\tilde{A})$, whereas the repulsive diabatic S_2 correlates to the ground phenylthiyl radical, $C_6H_5S\cdot(\tilde{X})$, at the asymptotic limit.[11,12] Relative yields of these two channels represent the nonadiabatic transition probability of the reactive flux at the S_0/S_2 conical intersection. Namely, the relative yield of the $C_6H_5S\cdot(\tilde{X})$ channel increases as the nonadiabatic transition probability increases. The energetic difference between the $C_6H_5S\cdot(\tilde{A})$ + $CD_3\cdot$ ($\upsilon = 0$) and $C_6H_5S\cdot(\tilde{X})$ + $CD_3\cdot$ ($\upsilon = 0$) channels is only ~8.6 kcal/mol,[23] and the translational energy measurement of the nascent $CD_3\cdot$ ($\upsilon = 0$) product gives the precise branching ratio of those two distinct reaction channels.

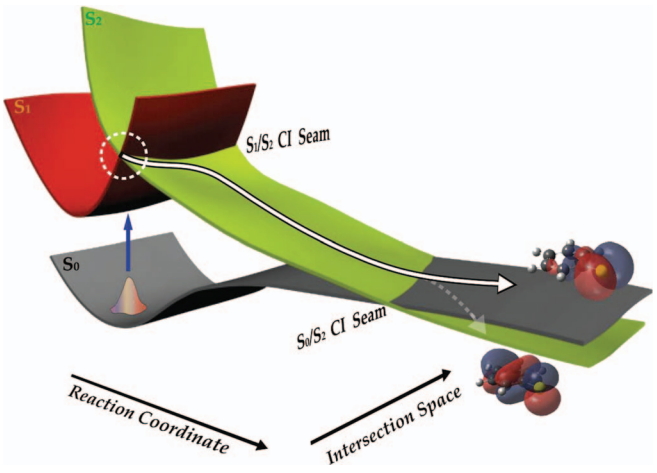

FIG. 1. Potential energy surfaces of three lowest singlet states (S_0, S_1, and S_2) of thioanisole along the S–CD_3 bond dissociation coordinate. The conical intersection seam is generated along the ($N^{int}-2$) dimensional intersection space which is orthogonal to the branching plane. The S_1–S_0 optical excitation at dynamic resonances prepares the reactive flux near the S_1/S_2 conical intersection seam, leading to the increase of the nonadiabatic transition probability.

In Fig. 2, the R2PI spectrum shows well-resolved S_1 vibronic structures of $C_6H_5SCD_3$ up to ~1100 cm^{-1} above the origin. In the higher energy region, the R2PI signal was observed to diminish and disappear at ~1500 cm^{-1} above the origin. However, in the PHOFEX spectrum in which the nascent $CD_3\cdot$ ($\upsilon = 0$) fragment yield is monitored as a function of the S_1–S_0 excitation energy, the intensity pattern shows the opposite behavior. Namely, the $CD_3\cdot$ fragment yield increases at ~1100 cm^{-1} above the origin, showing intense and complicated spectral features in the higher energy region where the R2PI signal is practically absent. These spectral patterns are very similar to those found for $C_6H_5SCH_3$,[12] indicating that there exists a turning point in this energy region where the photodissociation mechanism changes dramatically. The translational energy of the nascent $CD_3\cdot$ ($\upsilon = 0$) fragment has been measured at each S_1 vibronic band using the velocity-map ion imaging method.[12] The resultant $CD_3\cdot^+$ image reveals two distinct inner and outer rings corresponding to the $C_6H_5S\cdot(\tilde{A})$ + $CD_3\cdot$ ($\upsilon = 0$) and $C_6H_5S\cdot(\tilde{X})$ + $CD_3\cdot$ ($\upsilon = 0$) channels, respectively.[11,12] The $\tilde{X}/\tilde{A}$ branching ratio is then estimated from the relative intensity of the two rings, Fig. 2. This ratio is ~0.07 at the S_1 origin band and shows a gradual increase upon increasing S_1 internal energy, giving a value of ~0.15 when the S_1 internal energy is ~1500 cm^{-1}. Strikingly, however, the $\tilde{X}/\tilde{A}$ branching ratio increases at four distinct S_1 vibronic bands, namely, giving sharp peak values of ~0.33 at 656 cm^{-1}, ~0.38 at 705 cm^{-1}, ~0.43 at 708 cm^{-1}, and ~0.20 at 755 cm^{-1}.

In order to interrogate the nature of the S_1 vibronic bands associated with dynamic resonances, we carried out a (1+1′) MATI experiment, Fig. 3. Since the cationic ground state is bound and well-defined, assignments to cationic ground vibrational modes are straightforward when comparing with *ab initio* calculation results. MATI spectra reflect nuclear displacements associated with the particular S_1 vibronic state used as an intermediate state in the stepwise (1+1′) ionization process according to the Franck-Condon principle,[27,28] and thus assignments of cationic bands provide the nature of the corresponding S_1 vibrational bands. In the MATI spectrum in which the S_1–S_0 origin band was taken as an intermediate state, the D_0–S_1 origin band is most strongly observed. In this spectrum, all MATI spectral peaks other than the D_0–S_1 origin band appear as weak signals, indicating that there is little structural change of thioanisole-d_3 occurs upon the D_0–S_1 ionization process. Most vibrational bands follow the propensity rule of $\Delta\nu = 0$. It is found that the S_1 bands that give dynamic resonances correspond to C–S–CD_3 symmetric stretching (ν_s) at 656 cm^{-1}, C–S–CD_3 asymmetric stretching (7a) at 705 cm^{-1}, and CD_3 wagging ($\beta_{as}CD_3$) at 755 cm^{-1} (see the supplementary material[32]). In the MATI spectrum taken via the S_1 708 cm^{-1} band, however, three distinct D_0 vibrational bands corresponding to $7a^+$, ($\tau^+ + \nu_s{}^+$), and $\beta_{as}CD_3{}^+$ modes are found to be active, where τ^+ is associated with torsion along the dihedral angle between the phenyl moiety and the S–CD_3 bond axis. In the harmonic approximation, the multi-mode character of the 708 cm^{-1} band is hardly rationalized. Nonetheless, this indicates that the

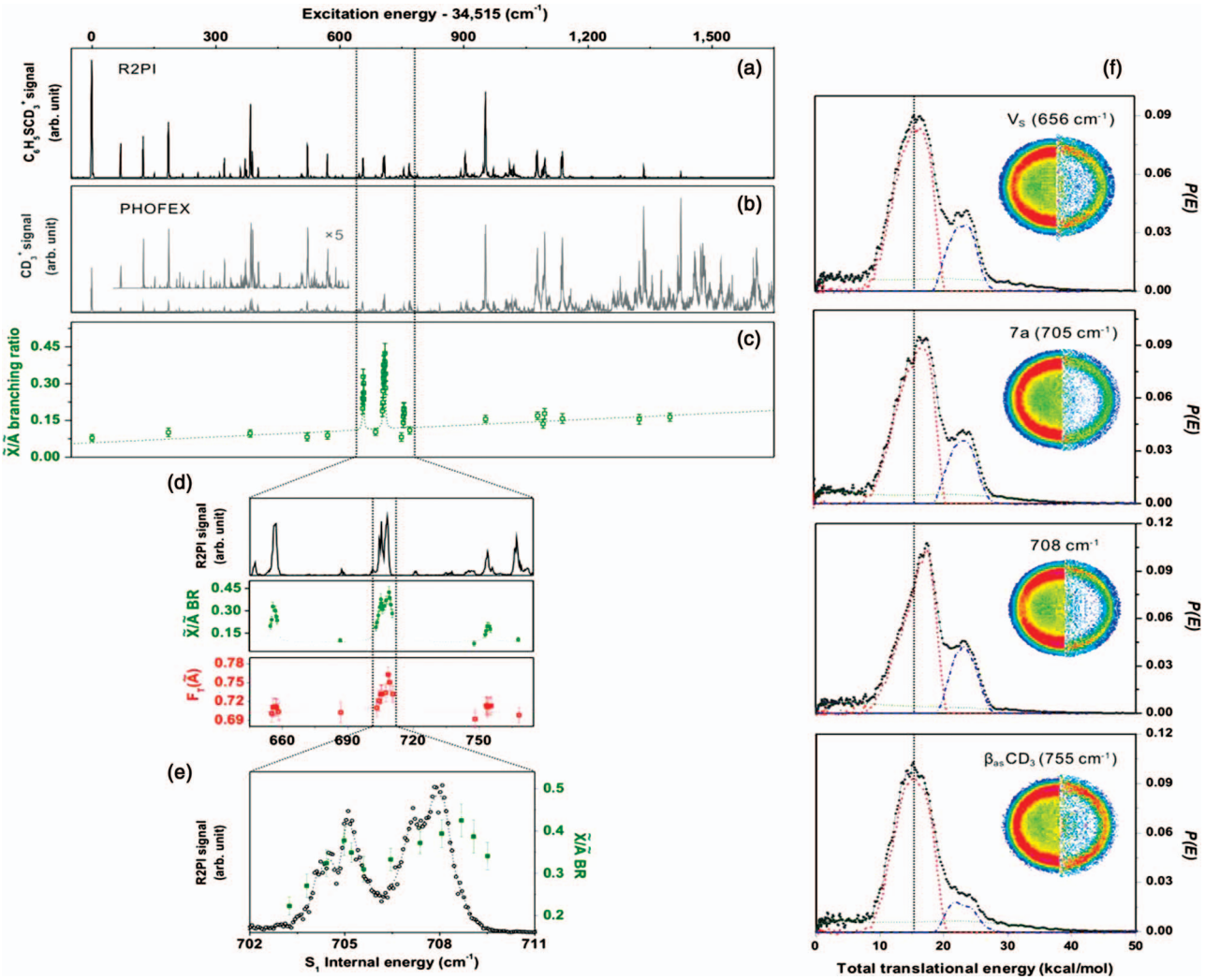

FIG. 2. (a) R2PI spectrum of the jet-cooled thioanisole-d_3, (b) PHOFEX spectrum taken by monitoring the $\cdot CD_3$ ($\nu = 0$) fragment yield as a function of the excitation energy, (c) the $\tilde{X}/\tilde{A}$ branching ratios estimated from the translational distributions of the $\cdot CD_3$ fragment, and (d) the enlarged view of the R2PI spectrum, $\tilde{X}/\tilde{A}$ branching ratio, and translational energy partitioning ratio for $\tilde{A}(F_T(\tilde{A}))$. The available energy ($E_{avl}$) is determined by the relation of $E_{avl} = h\nu - D_0 - \Delta$, where $h\nu$ is the excitation energy, D_0 is the phS–CD_3 bond dissociation energy of 73.5 kcal/mol, and Δ is the energy gap of 8.6 kcal/mol between $\tilde{X}$ and $\tilde{A}$ states of $C_6H_5S\cdot$.[23] (e) Enlarged view of the R2PI spectrum and $\tilde{X}/\tilde{A}$ branching ratio around the 708 cm^{-1} region. (f) Total translational energy distributions deduced from CD_3^+ images at S_1 internal energies of 656 (ν_s), 705 (7a), 708, and 755 ($\beta_{as}CD_3$) cm^{-1} bands. Raw (left) and reconstructed (right) images are also shown. The broad background signal shows the quadratic dependence on the pump laser intensity indicating that it is due to two-photon absorption of the parent molecule. The nascent $\cdot CD_3$ radical ($\nu = 0$) was probed by (2+1) ionization at 333 nm via $3p^2\ A_2''$ state. Other experimental details are given in Ref. 12.

nuclear configuration accessed by the 708 cm^{-1} band contains that reached by the C–S–CD_3 symmetric stretching, C–S–CD_3 asymmetric stretching, and CD_3 wagging modes simultaneously.

Dynamic resonances result from the more efficient nonadiabatic passage of the reactive flux through the S_0/S_2 conical intersection seam, giving the higher $\tilde{X}/\tilde{A}$ product branching ratio. Direct access to the S_1/S_2 conical intersection seam at dynamic resonance frequencies minimizes the vibrational energy flow into the asymmetric coupling mode such as the C–C–S–CD_3 torsion, allowing for the reactant flux to proceed in the closer proximity of the S_0/S_2 conical intersection seam. This in turn leads to the higher nonadiabatic transition probability as the reactive flux becomes less dispersed, for instance, along the non-planar degrees of freedom. The experimental fact that the $\tilde{X}/\tilde{A}$ product branching ratio shows sharp peak values at four distinct S_1 vibronic bands thus indicates these excitations bring the reactant to nuclear configurations near the S_1/S_2 conical intersection seam. Namely, facets of the multi-dimensional conical intersection seam are revealed by the multiple dynamic resonances at different vibronic excitations. Bands showing dynamic resonances are not particularly broader than other vibronic bands, suggesting that the increase of the S_1/S_2 coupling strength may not necessarily correlate with the increase of the reaction rate since the S_1/S_2 conical intersection seam is multi-dimensional in nature.

Although a full description of the conical intersection seam requires the complete knowledge of the potential energy surfaces along all internal degrees of freedom, it may be quite useful to describe the seam in the reduced dimensionality as we focus here on the S–CD_3 bond dissociation pathway. Four internal coordinates were chosen to

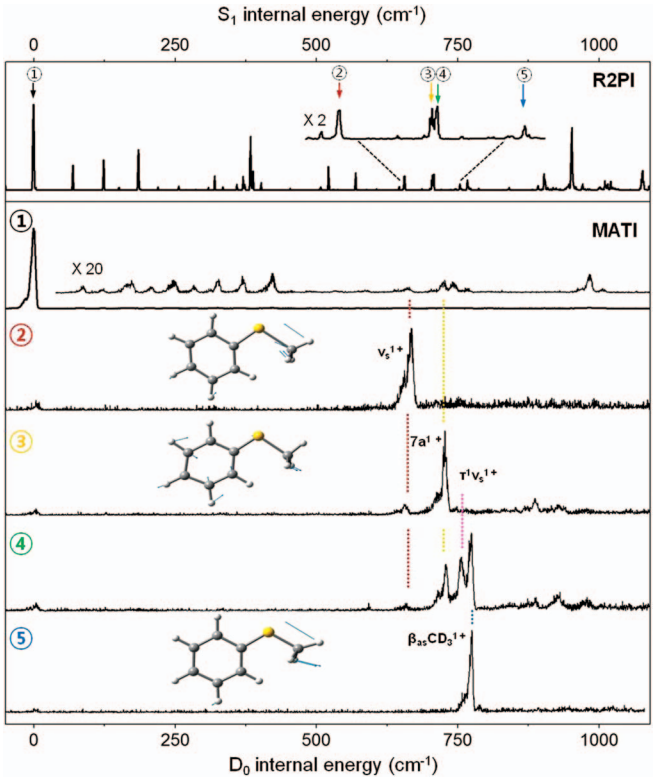

FIG. 3. Upper trace: R2PI spectrum of thioanisole-d_3, Lower traces: (1+1′) MATI spectra taken via the S_1 origin, 655 (ν_s), 705 (7a), 708, and 755 ($\beta_{as}CD_3$) cm^{-1} bands as intermediate states. Nuclear displacement vector descriptions of corresponding normal modes of D_0 calculated at the B3LYP/6-311++G(3df,3pd) level are shown.

describe the nuclear configurations of the conical intersection seam. These are d(C–SCD_3), d(CS–CD_3), γ(C–S–CD_3), and γ(S–C–$D_{(3)}$), where d and γ represent bond length and bending angle, respectively (Table I). We carried out *ab initio* calculations (SA4-CASSCF(12,11)/6-311++G(d,p)) to find out the S_1/S_2 conical intersection seam in the reduced dimensionality accordingly. The structural parameters of the phenyl moiety are fixed whereas other internal degrees of freedom including d(C–SCD_3), d(CS–CD_3), γ(C–S–CD_3), and γ(S–C–$D_{(3)}$) are varied. In Fig. 4, the resultant S_1/S_2 conical intersection seam is depicted as a line connecting degenerate points where the difference between the S_1 and S_2 states is calculated to be less than 5 cm^{-1}. Here, the branching plane of the g and h vectors parallel to the S–CD_3 elongation and the C–C–S–CD_3 dihedral angle coordinates, respectively, provides a platform for the conical intersection seam (Table I). It should be noted that the conical intersection points on the seam are energetically overestimated. The S_1/S_2 MECI point, calculated at the same level but after the full optimization of the phenyl moiety, is found to be located at a lower energy than the lowest point on the conical intersection seam calculated in the reduced dimensionality. The g and h vectors of MECI are found to remain identical. The energy of the conical intersection seam decreases with increasing of the d(CS–CD_3) and γ(S–C–$D_{(3)}$) values, whereas it increases with the increase of γ(C–S–CD_3). The conical intersection seam is quite well defined with respect to these three coordinates as its energy shows the monotonic change with the change of each variable. Interestingly, the nuclear configuration that converges to minimum energies along these three coordinates coincides with that of MECI, suggesting that the conical intersection seam calculated in the reduced dimensionality adequately describes the topological aspect of the potential energy surface near the S_1/S_2 conical intersection. Along the d(C–SCD_3) coordinate, however, the conical intersection seam is relatively poorly defined, meaning that the seam is scattered throughout a wide range of d(C–SCD_3) values. This is ascribed to the phenyl moiety not being optimized in the calculation.

To visualize how the initial optical transition directly accesses the S_1/S_2 conical intersection seam, we examined the nuclear configurations accessed by the S_1 vibronic excitations associated with dynamic resonances. Here, the energetics of the calculated conical intersection seam is not considered in the comparison with the experiment. The D_0 state gives the square of the coefficients in the expansion of the wavefunction in terms of normal modes for the corresponding S_1 vibronic state. This is well demonstrated in the MATI spectra, Fig. 3. Nuclear displacement vectors of normal modes for the C–S–CD_3 symmetric stretching (ν_s) at 656 cm^{-1}, C–S–CD_3 asymmetric stretching (7a) at 705 cm^{-1}, and CD_3 wagging at 755 cm^{-1} are projected onto the two-dimensional coordinates of d(CS–CD_3) and γ(S–C–$D_{(3)}$) (or d(CS–CD_3) and γ(C–S–CD_3)) in Fig. 4. Nuclear configurations spanned by the 7a mode, for instance, are found to partly overlap with those of the conical intersection seam in both projections into d(CS–CD_3)–γ(S–C–$D_{(3)}$) and d(CS–CD_3)–γ(C–S–CD_3) coordinates. Meanwhile, the ν_s mode shows the overlap with the conical intersection seam only when its nuclear configuration is projected onto the d(CS–CD_3) and γ(C–S–CD_3) coordinates. This helps explain why the $\tilde{X}/\tilde{A}$ branching ratio of ~0.38 observed for the 7a mode excitation is slightly higher than that of ~0.33 observed for the ν_s excitation. Specifically, the greater the extent of the overlap of the vibrational wavefunction with the conical intersection seam, the greater the increase in the portion of the reactant flux passing in the vicinity of the conical intersection seam. This then gives higher nonadiabatic transition probability. On the other hand, the nuclear configurations spanned by the $\beta_{as}CD_3$ mode excitation do not overlap with the conical intersection seam, even though its $\tilde{X}/\tilde{A}$ branching ratio of ~0.20 at 755 cm^{-1} is only slightly higher than the average value of ~0.12.

The 708 cm^{-1} band that gives the $\tilde{X}/\tilde{A}$ branching ratio of ~0.43 has the multi-mode character of the C–S–CD_3 symmetric stretching, C–S–CD_3 asymmetric stretching, and CD_3 wagging modes. Intriguingly, all of these individual modes show dynamic resonances in the $\tilde{X}/\tilde{A}$ branching ratio. Thus, the 708 cm^{-1} vibrational wavefunction, which could be constructed as a linear combination of ν_s, 7a, and $\beta_{as}CD_3$ modes, has the greatest overlap with the conical intersection seam to give the highest $\tilde{X}/\tilde{A}$ branching ratio. Energetically, the 708 cm^{-1} band cannot be a combination mode of these S_1 fundamental modes in the harmonic approximation. Rather, this band may be a unique oscillatory mode for which the associated nuclear displacement vectors cannot be represented by one single D_0 vibrational mode. In other words, the potential energy surface along this particular coordinate could

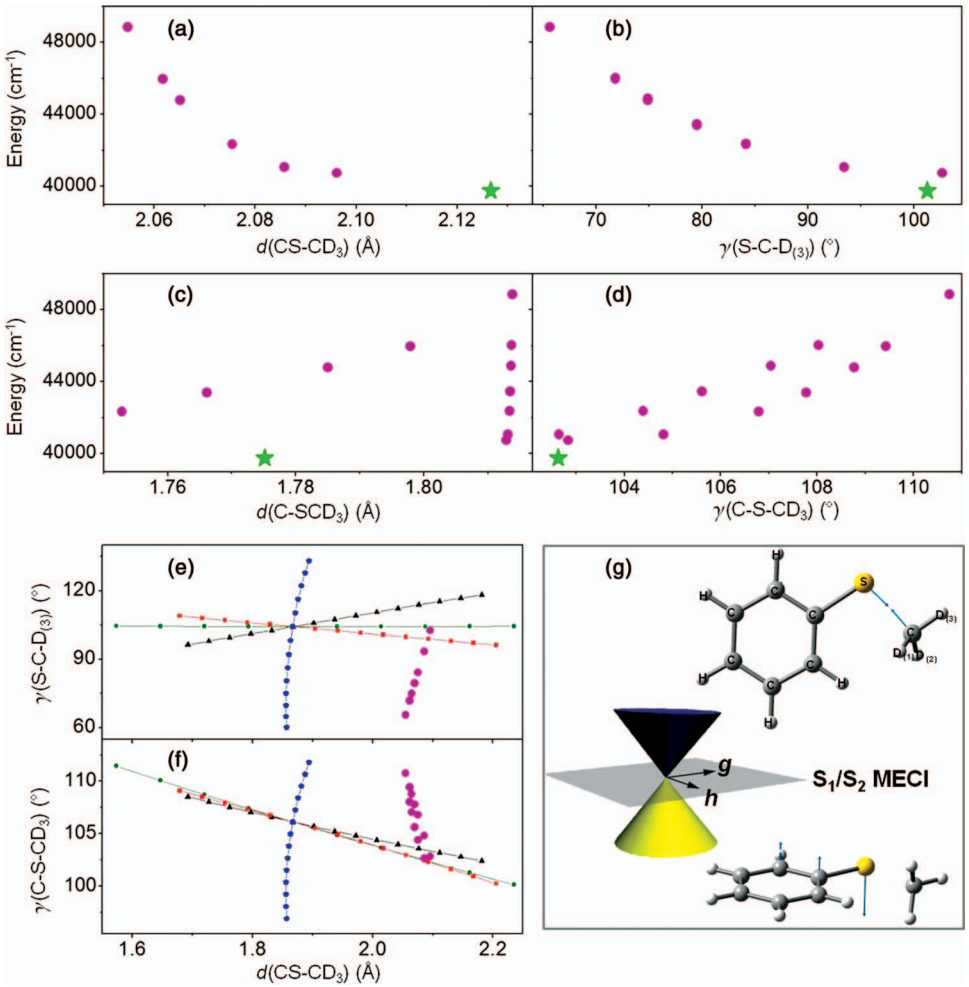

FIG. 4. Calculated energies of the conical intersection seam are plotted versus the variation of (a) d(C–SCD$_3$), (b) d(CS–CD$_3$), (c) γ(C–S–CD$_3$), or (d) γ(S–C–D$_{(3)}$). Energy values are relative to the S$_0$ state. Filled circles (magenta) are electronically degenerate points of S$_1$ and S$_2$, whereas the star (green) represents the MECI. Nuclear configurations spanned by the normal mode nuclear displacement vectors are represented as projections onto the (e) d(CS–CD$_3$)–γ(S–C–D$_{(3)}$) or (f) d(CS–CD$_3$)–γ(C–S–CD$_3$) coordinates. Normal mode descriptions for ν_s, 7a, and β_{as}CD$_3$ are represented by filled triangles (black line), filled squares (red line), and filled pentagons (blue line), respectively. Filled circles (green line) indicate nuclear configurations which are constructed from the linear combination of displacement vectors of ν_s, 7a, and β_{as}CD$_3$ modes with a respective weighting factor of 0.4:0.5:0.1. The gradient difference (g) and nonadiabatic coupling (h) vectors of the branching plane for the conical intersection seam are depicted (g).

be strongly perturbed by the nearby S$_1$/S$_2$ conical intersection seam which may also act as a guiding path for the reactant flux along the S–CD$_3$ dissociation reaction. This particular vibronic band may then represent "a bound state embedded in the continuum" generated by the conical intersection, predicted by Neumann and Wigner[29] in 1929 and extended theoretically to photodissociation reactions by Cederbaum and colleagues.[30,31] Here, the bound state in the continuum is meant to be a state which is supposed to be unbound on the diabatic repulsive S$_2$ surface and yet bound due to interference caused by the nearby conical intersection. A simple model for the diabatic V$_b$ (S$_1$) and V$_c$ (S$_2$) potentials is as follows:

$$V_b(S_1)\frac{1}{2}\sum_{i=1}^{(3N-6)}\omega_i {x_i}^2,$$

$$V_c(S_2) = \varepsilon \exp^{-\beta(x'_1)} + \frac{1}{2}\sum_{i=2}^{(3N-6)}\omega'_i {x'_i}^2 + \Delta.$$

In these harmonic potentials, the S$_1$ state is bound for all internal degrees of freedom, $\{x_i, i = 1 - (3N-6)\}$, whereas the S$_2$ state is repulsive along one particular single mode (x'_1) but bound for all other internal modes, $\{x'_i, i = 2 - (3N-6)\}$. Here, ε and β are parameters for the shape of the repulsive potential whereas Δ is the energy gap between the energetic minima of S$_1$ and S$_2$. Since the normal modes for S$_1$ is expected to differ from those of S$_2$, the x'_1 mode along which S$_2$ is repulsive could be described as a linear combination of S$_1$ normal modes. Also, the gradient difference vector (g) of the branching plane as a platform of the S$_1$/S$_2$ conical intersection is likely to be parallel to neither the single S$_1$ nor the S$_2$ normal mode. The coupling of S$_1$ and S$_2$ should therefore be taken into account in the multi-dimensional normal mode space. As the S$_1$ mode is optically active in the energy range studied here, it is plausible then that the 708 cm^{-1} band as "a bound state embedded in the continuum" is manifested as a linear combination of relevant optically active S$_1$ modes of ν_s, 7a, and β_{as}CD$_3$, representing the nuclear configuration on the S$_1$/S$_2$ conical intersection seam which eventually leads to S–CD$_3$ bond rupture. It should be noted that the transfer of the internal energy into the translational

energy at the 708 cm^{-1} resonance band also stands out, which is clearly manifested in the experimental product kinetic energy distribution. Namely, at the dynamic resonance at 708 cm^{-1}, the translational energy distribution shifts abruptly to higher energy, giving a somewhat shaper peak seen in the plot of the product translational energy partitioning ratio as a function of the excitation energy, Fig. 2. A sudden change in the translational energy distribution of products within an extremely narrow range of the given energy is very uncommon. This observation strongly indicates that the 708 cm^{-1} band represents the nuclear configuration on the conical intersection seam bearing the multi-dimensional nature of the reaction coordinate. Included in this growing picture, the three other dynamic resonances observed at ν_s (656 cm^{-1}), 7a (705 cm^{-1}), and $\beta_{as}CD_3$ (755 cm^{-1}) may be mere consequences from the projection of the 708 cm^{-1} resonance band into the S_1 normal mode space. However, further work such as assessing lifetime measurements for individual resonances or undertaking calculations of multi-dimensional nonadiabatic coupling will be critical.

In our recent report on thioanisole ($C_6H_5SCH_3$),[12] a striking resonance in the $\tilde{X}/\tilde{A}$ branching ratio is observed only at the 722 cm^{-1} band assigned to the asymmetric C–S–CH_3 stretching (7a) mode. Since the location and energetics of the S_1/S_2 conical intersection seam are expected to be only slightly affected by the deuterium incorporation, a similar experimental result was expected for $C_6H_5SCD_3$. However, as above, we observed additional dynamic resonances at three more distinct bands for $C_6H_5SCD_3$. The overlap of the vibrational wavefunction with the conical intersection seam seems to be extremely sensitive to nuclear displacement associated with each normal mode and energetics. In this sense, why dynamic resonance is not observed in the C–S–CH_3 symmetric stretching mode (ν_s) and CH_3 wagging mode ($\beta_{as}CH_3$) in the $C_6H_5SCH_3$ dissociation could originate from subtle differences of the corresponding normal modes in terms of the detailed nuclear displacement vectors in the mass-weighted coordinate. The ν_s normal mode of $C_6H_5SCH_3$ is different from that of $C_6H_5SCD_3$; furthermore, the nuclear displacement vector does not access the conical intersection seam directly (see the supplementary material[32]). Energetically, the $\beta_{as}CH_3$ vibrational energy in $C_6H_5SCH_3$ is high; the corresponding excitation region should be remote from the conical intersection seam. Importantly, the 722 cm^{-1} band of S_1 $C_6H_5SCH_3$, which had been previously assigned to the 7a mode, might represent "a bound state embedded in continuum," judging from the similarity of its mode dynamics to that of the 708 cm^{-1} band of S_1 $C_6H_5SCD_3$. However, further studies are required to confirm these speculations.

IV. CONCLUSION

Herein, we were able to locate the conical intersection seam from experimental observation of multiple dynamic resonances in the product branching ratio as a result of the change of the nonadiabatic transition probability depending on the initial nuclear configuration of the reactant flux. Experimental findings concerning the nuclear configurations responsible for the degenerate excited electronic states reveal for the first time the multi-dimensional nature of the conical intersection seam for a chemical reaction involving a polyatomic system. The bound state embedded in continuum generated by the conical intersection has been experimentally observed for the first time in the photodissociation reaction. It is extremely interesting and important to reveal that the nuclear configurations of the initial reactant flux are critical in controlling the nonadiabatic reaction dynamics occurring on the excited electronic states through strong coupling of nuclear and electronic motions beyond the Born-Oppenheimer approximation. These experimental findings lead towards a more thorough understanding of and the ability to control the intricacies of the chemical reactions in excited states.

ACKNOWLEDGMENTS

This work was supported by the National Research Foundation (NRF) grant funded by the Korean government (2012-0005607, SRC 2012-0000779). S. Han appreciates the National Junior research fellowship (2011-0001762).

[1] M. Born and R. Oppenheimer, Ann. Phys. **389**, 457 (1927).
[2] W. Domcke, D. R. Yarkony, and H. Köppel, *Conical Intersections: Electronic Structure, Dynamics and Spectroscopy* (World Scientific, Singapore, 2004), and references therein.
[3] D. R. Yarkony, Rev. Mod. Phys. **68**, 985 (1996).
[4] G. A. Worth and L. S. Cederbaum, Annu. Rev. Phys. Chem. **55**, 127 (2004).
[5] H. Köppel, W. Domcke, and L. S. Cederbaum, Adv. Chem. Phys. **57**, 59 (2007).
[6] J. C. Tully, J. Chem. Phys. **137**, 22A301 (2012).
[7] T. S. Venkatesan, S. G. Ramesh, Z. Lan, and W. Domcke, J. Chem. Phys. **136**, 174312 (2012).
[8] A. Migani, L. Blancafort, M. A. Robb, and A. D. DeBellis, J. Am. Chem. Soc. **130**, 6932 (2008).
[9] T. Mori and T. J. Martinez, J. Chem. Theory Comput. **9**, 1155 (2013).
[10] D.-S. Ahn, J.-M. Lee, J.-M. Choi, K.-S. Lee, S. J. Baek, K. Lee, K.-K. Baeck, and S. K. Kim, J. Chem. Phys. **128**, 224305 (2008).
[11] J. S. Lim, I. S. Lim, K.-S. Lee, D.-S. Ahn, Y. S. Lee, and S. K. Kim, Angew. Chem., Int. Ed. **45**, 6290 (2006); I. S. Lim, J. S. Lim, Y. S. Lee, and S. K. Kim, J. Chem. Phys. **126**, 034306 (2007); J. S. Lim, Y. S. Lee, and S. K. Kim, Angew. Chem., Int. Ed. **47**, 1853 (2008).
[12] J. S. Lim and S. K. Kim, Nat. Chem. **2**, 627 (2010).
[13] M. N. R. Ashfold, B. Cronin, A. L. Devine, R. N. Dixon, and M. G. D. Nix, Science **312**, 1637 (2006).
[14] G. M. Roberts, D. J. Hadden, L. T. Bergendahl, A. M. Wenge, S. J. Harris, T. N. V. Karsili, M. N. R. Ashfold, M. J. Paterson, and V. G. Stavros, Chem. Sci. **4**, 993 (2013).
[15] A. L. Devine, M. G. D. Nix, R. D. Dixon, and M. N. R. Ashfold, J. Phys. Chem. A **112**, 9563 (2008).
[16] M. L. Hause, Y. H. Yoon, A. S. Case, and F. F. Crim, J. Chem. Phys. **128**, 104307 (2008).
[17] C.-M. Tseng, Y. T. Lee, and C.-K. Ni, J. Chem. Phys. **121**, 2459 (2004).
[18] A. Stolow, Int. Rev. Phys. Chem. **22**, 377 (2003).
[19] H. J. Wörner, J. B. Bertrand, B. Fabre, J. Higuet, H. Ruf, A. Dubrouil, S. Patchkovskii, M. Spanner, Y. Mairesse, V. Blanchet, E. Mével, E. Constant, P. B. Corkum, and D. M. Villeneuve, Science **334**, 208 (2011).
[20] D. Polli, P. Altoè, O. Weingart, K. M. Spillane, C. Manzoni, D. Brida, G. Tomasello, G. Orlandi, P. Kukura, R. A. Mathies, M. Garavelli, and G. Cerullo, Nature (London) **467**, 440 (2010).
[21] Y.-I. Suzuki, T. Fuji, T. Horio, and T. Suzuki, J. Chem. Phys. **132**, 174302 (2010).
[22] X. Zhou, P. Ranitovic, C. W. Hogle, J. H. D. Eland, H. C. Kapteyn, and M. M. Murnane, Nat. Phys. **8**, 232 (2012).
[23] J. B. Kim, T. I. Yacovitch, C. Hock, and D. M. Neumark, Phys. Chem. Chem. Phys. **13**, 17378 (2011).
[24] A. T. J. B. Eppink and D. H. Parker, Rev. Sci. Instrum. **68**, 3477 (1997).
[25] D. W. Chandler and P. L. Houston, J. Chem. Phys. **87**, 1445 (1987).

[26]V. Dribinski, A. Ossadtchi, V. A. Mandelshtam, and H. Reisler, Rev. Sci. Instrum. **73**, 2634 (2002).
[27]K.-W. Choi, S. Choi, S. J. Baek, and S. K. Kim, J. Chem. Phys. **126**, 034308 (2007).
[28]S. J. Baek, K.-W. Choi, Y. S. Choi, and S. K. Kim, J. Chem. Phys. **117**, 2131 (2002).
[29]J. von Neumann and E. Wigner, Phys. Z. **30**, 467 (1929).
[30]L. S. Cederbaum, R. S. Friedman, V. M. Ryaboy, and N. Moiseyev, Phys. Rev. Lett. **90**, 013001 (2003).
[31]R. S. Friedman, I. Podzielinski, L. S. Cederbaum, V. M. Ryaboy, and N. Moiseyev, J. Phys. Chem. A **106**, 4320 (2002).
[32]See supplementary material at http://dx.doi.org/10.1063/1.4863449 for experimental details, computational details, R2PI and MATI spectra, tables of vibrational frequencies with assignments, geometries.